ACS Catalysis
Research Article
pubs.acs.org/acscatalysis

Nitrogen-Doped Hollow Carbon Spheres as a Support for Platinum-Based Electrocatalysts

Carolina Galeano,*[,†,§] Josef C. Meier,[‡,§] Mario Soorholtz,[†] Hans Bongard,[†] Claudio Baldizzone,[‡] Karl J. J. Mayrhofer,[‡] and Ferdi Schüth*[,†]

[†]Department of Heterogeneous Catalysis, Max-Planck-Institut für Kohlenforschung, Kaiser-Wilhelm-Platz 1, 45470 Mülheim an der Ruhr, Germany

[‡]Department of Interface Chemistry and Surface Engineering, Max-Planck-Institut für Eisenforschung, Max-Planck-Strasse 1, 40237 Düsseldorf, Germany

Supporting Information

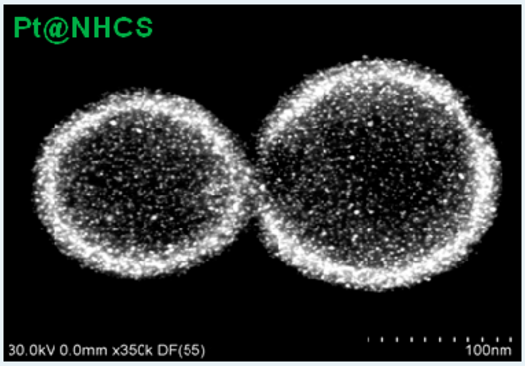

ABSTRACT: Platinum and platinum alloys supported on carbon materials are the state of the art electrocatalysts for the essential oxygen reduction reaction (ORR) in low-temperature fuel cells. The limited stability of such materials under the often detrimental operation conditions of fuel cells still remains a critical issue to improve. In this work, we explore the impact of nitrogen-doped carbon supports on the activity and stability of platinum-based fuel cell catalysts. We present a nitrogen-doped mesostructured carbon material, nitrogen-doped hollow carbon spheres (NHCS), as a support for platinum-based electrocatalysts. A detailed study of the electrochemical activity and stability was carried out for two Pt@NHCS materials i.e., as-made material (Pt@NHCS) with a Pt particle size smaller than 2 nm and the corresponding material after thermal treatment at 850 °C (Pt@NHCS$_{\Delta T}$) with a Pt particle size of ca. 2−3 nm. Activity in the ORR was studied by rotating disc electrode (RDE) thin-film measurements, and electrocatalyst stability was evaluated by accelerated aging tests under simulated start−stop conditions. The performance of the NHCS-based materials was compared to the two corresponding nitrogen-free materials as well as to a standard Pt/Vulcan catalyst. The underlying degradation mechanisms of Pt@NHCS materials were investigated via identical location electron microscopy. Our results conclusively show that nitrogen doping of the carbon supports can offer benefits for achieving high initial mass activities due to improved high platinum dispersion; however, it was not found to necessarily lead to an improvement of the catalyst stability.

KEYWORDS: *electrocatalysis, nitrogen-doped carbon, platinum nanoparticles, stability, fuel cells*

INTRODUCTION

Electrochemical processes are expected to play a key role in the implementation of sustainable energy technologies in our future energy systems.[1] Fuel cells hold great promise for the electrocatalytic chemical energy conversion of small molecules as energy carriers, such as hydrogen, methanol, and ethanol. Over the last decades, fuel cell technology experienced a significant progress, bringing it closer to large scale applications.[2−4] In order to obtain cost-competitive materials, particular attention has been paid to the improvement of electrocatalyst activity for the essential oxygen reduction reaction (ORR). Although nanostructured platinum or platinum alloy catalysts were intensively studied in this respect,[5−17] the stability of such materials under the often harsh operation conditions of fuel cells still remains a challenge. Thus, improvement of electrocatalyst durability currently is one of the most important fundamental issues to address. The degradation of ORR electrocatalysts has been demonstrated to be particularly critical under nonideal transient operation conditions, such as start-up/shut-down (start−stop) processes as well as local fuel starvation.[18−23] Under these conditions, the cathode can locally reach potentials as high as 1.5 V, causing oxidation of the carbon support as well as the dissolution, agglomeration, and detachment of the platinum nanoparticles.[21,24−30] To address this instability issue, several approaches have been proposed at the material level. For example, the use of graphitic carbon supports, such as carbon nanotubes[31−36] and graphitized carbon blacks,[23,37−39] has proven to be beneficial in reducing carbon corrosion. Furthermore, the use of tailored catalyst structures, such as mesostructured thin films[40] and nanostructured thin films (NSTF),[41−44] significantly reduces the intrinsic instability issues of nanoparticle-based catalysts. Recently, we have shown that mesostructured carbon supports offer significant improvement in catalyst stability of nanoparticle-based catalysts.[45] In particular, we demonstrated that the confinement

Received: March 17, 2014
Revised: September 1, 2014
Published: September 8, 2014

ACS Publications © 2014 American Chemical Society

dx.doi.org/10.1021/cs5003492 | *ACS Catal.* 2014, 4, 3856−3868

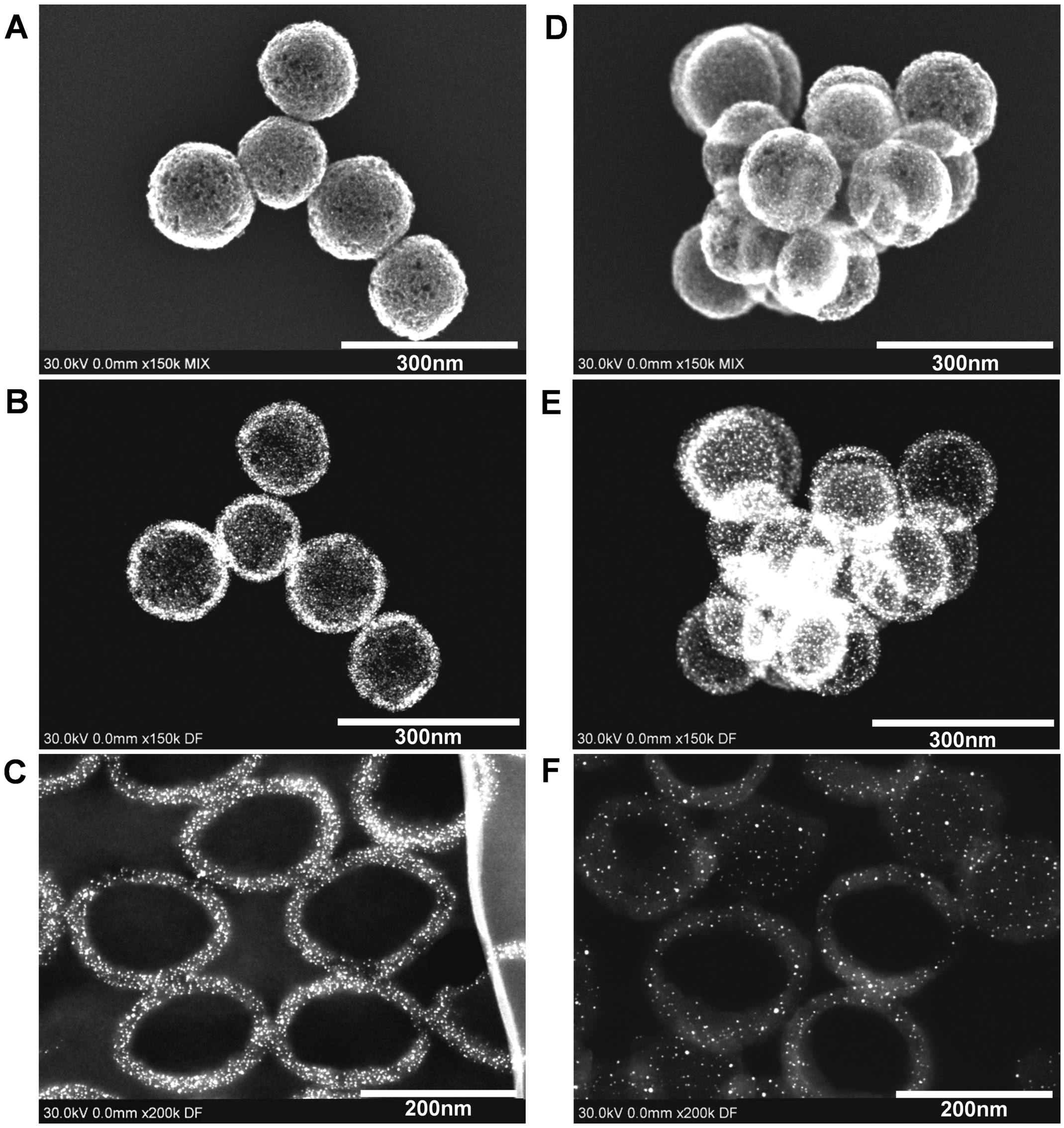

Figure 1. HR-SEM (A,D), DF-STEM (B,E), and DF-STEM micrographs of cross sections (C,F) of Pt@NHCS as-made (A−C) and Pt@NHCS$_{\Delta T}$ after thermal treatment at 850 °C (D−F).

of the electrocatalyst nanoparticles in tailored mesostructured graphitic supports, that is, hollow graphitic spheres (HGS), slows down detachment and agglomeration processes of Pt nanoparticles under simulated start−stop operation conditions. This stabilization effect has been associated with the efficient separation and encapsulation of the Pt nanoparticles in the mesopore system, in combination with an improved graphitization degree of HGS, without limiting their accessibility for electrochemical reactions.

Nitrogen-doped carbons have been proposed as metal-free catalysts as well as metal-based catalyst supports for electrochemical energy conversion systems.[46−56] For metal-based catalyst materials, it has been suggested that carbon materials can be systematically doped with nitrogen to generate favorable metal−support interactions, which significantly enhance catalyst activity and stability.[57−59] Previous studies propose that nitrogen functional groups introduced into carbon supports influence three main aspects of the catalyst−support boundary:[57] (i) modified nucleation and growth kinetics during catalyst nanoparticle deposition, which results in smaller catalyst particle size and increased dispersion, (ii) increased catalyst−support chemical bonding, which might result in enhanced durability, and (iii) modification of the electronic structure of the catalyst nanoparticles, which might enhance intrinsic catalytic activity. Nitrogen doping methods can be divided into two main groups: *in situ doping* and *postsynthesis doping* methods.[57,59] On the one hand, pyrolysis of nitrogen-containing precursors[50−53,60−62] and chemical vapor deposition of nitrogen-containing compounds[46,55,63−65] are the most straightforward methods for *in situ doping*. On the other hand, *postsynthesis doping* methods involve the treatment at high temperatures of preformed carbon materials in a nitrogen containing atmosphere (e.g., NH_3).[66−69] This method has been widely used for nitrogen functionalization of carbon materials and usually requires the preoxidation of the carbon surface or the aid of transition metals for the incorporation of the nitrogen species into the carbon network. Although the chemical processes behind the different nitrogen doping methods are well understood, the nature of the introduced nitrogen active species and their effects on the resulting electrocatalytic properties are still highly controversial.

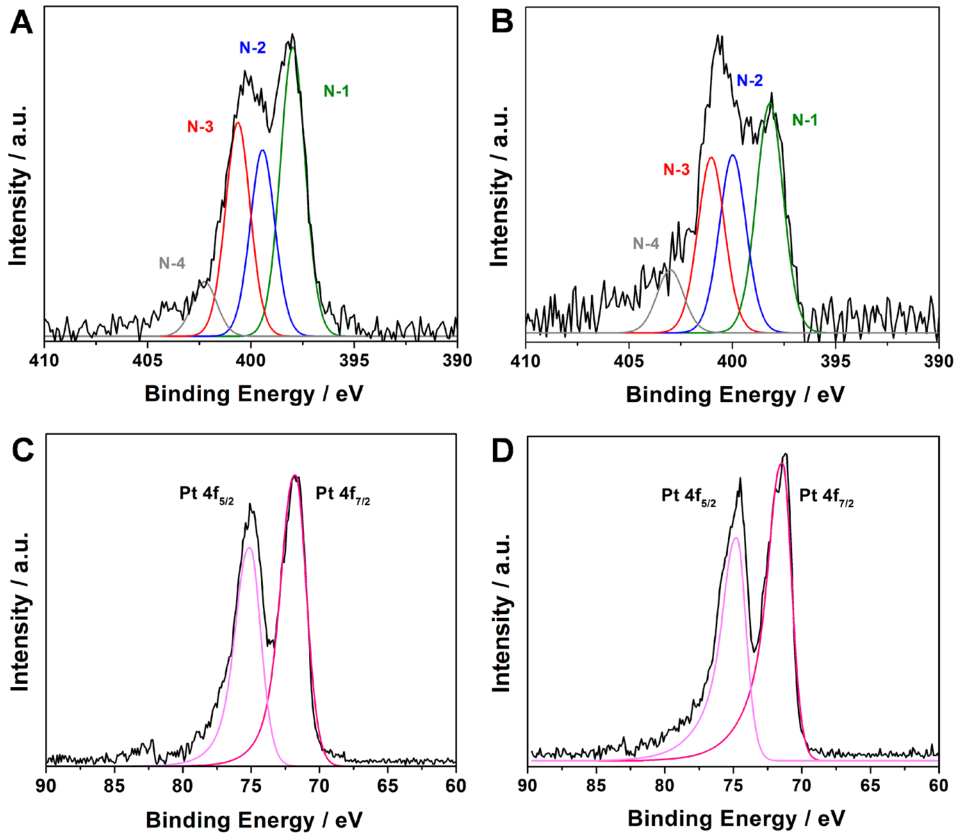

Figure 2. XPS N 1s and Pt 4f spectra of Pt@NHCS after reduction at 250 °C in H_2 (A,C) and Pt@NHCS$_{\Delta T}$ after thermal treatment at 850 °C in Ar (B,D). The carbonization of the NHCS support alone was done at 850 °C in Nitrogen. The black lines correspond to the raw spectra. The colored curves correspond to the deconvolutions of the fitted species. The deconvolutions are intended to provide a guide to the eye and do not represent any absolute assignment to the existing nitrogen species, because they may slightly change according to the initial parameters used for fitting.

In this work, we present nitrogen-doped hollow carbon spheres (NHCS) as a support for platinum based electrocatalysts. The NHCS were synthesized in analogy to the aforementioned hollow graphitic spheres (HGS) material.[45,70,71] NHCS was synthesized using polyacrylonitrile (PAN) as carbon precursor, while the previously reported HGS had been synthesized starting from polydivinylbenzene (PDVB) as carbon source. In both cases polymerization and a successive carbonization step at high temperatures results in the final carbon material with comparable structure (morphology and porosity), but in the case of NHCS, there are significant amounts of nitrogen functionalities and nongraphitized carbon. The use of PAN as precursor allows systematic tailoring of the nitrogen functionalities during the carbonization process.[60,72] Due to the properties of NHCS, this material is an excellent model support for exploring the impact of nitrogen doping on the activity and stability of platinum-based fuel-cell catalysts. Therefore, the electrochemical properties of platinum nanoparticles supported on NHCS were investigated in detail. The Pt@NHCS catalysts were synthesized using the same particle pore confinement pathway developed for the HGS system.[45] A detailed comparison of the electrochemical activity for the ORR via rotating disc electrode (RDE) thin-film measurements was carried out for the two Pt@NHCS materials (as-made and after thermal treatment) and the two corresponding nitrogen-free Pt@HGS materials as well as a standard Pt/Vulcan catalyst. Finally, to gain a fundamental understanding about the impact of nitrogen-doping on the durability of carbon support materials, accelerated aging tests were performed for all five catalysts to estimate the overall stability of the materials under simulated start–stop conditions. Additionally, to investigate the macroscopic stability behavior, the underlying degradation mechanisms of Pt@NHCS materials were investigated via identical location electron microscopy.

■ RESULTS AND DISCUSSION

Synthesis and Characterization of the Materials. Nitrogen-doped hollow carbon spheres (NHCS) were synthesized by nanocasting using nonporous core/mesoporous–shell silica spheres as exotemplate.[45] NHCS derived from carbonization of PAN at 850 °C consist of hollow spheres with a diameter of about 200 nm and a shell thickness of about 30 nm. The capillary condensation region of the nitrogen sorption isotherm (Figure S1A) presents a defined-volume uptake associated with the mesoporous structure of the shell. At high relative pressures, some capillary condensation associated with interparticle voids also occurs. The desorption branch has a pronounced hysteresis loop due to the contribution of the ink-bottle pore structure. The closure of the hysteresis loop occurs at ca. 0.44 P/P_0, close to the value where the meniscus becomes unstable. The presence of pores smaller than 4 nm is confirmed in both, adsorption and desorption, BJH (Barrett–Joyner–Halenda) pore size distributions (Figure S1A inset). The BJH pore size distribution determined from the desorption branch is characterized by a narrow peak centered at 3.8 nm, which is an artifact caused by the tensile-strength effect.[73,74] The BET (Brunauer–Emmett–Teller) surface area and total pore volume of NHCS are 1761 $m^2\ g^{-1}$ and 1.3 $cm^3\ g^{-1}$, respectively.

Table 1. Particle Size According to DF-STEM, Electrochemical Surface Area (ECSA), Specific Activity (SA), and Mass Activity (MA) of NHCS-Based Materials, HGS-Based Materials, and Standard Pt/Vulcan Comparison Material Determined in 0.1 M $HClO_4$[a]

			specific activity (mA cm^{-2})	mass activity (A mg_{Pt}^{-1})
catalyst	particle size (nm)	ECSA (m^2 g_{Pt}^{-1})	$HClO_4$	$HClO_4$
Pt@NHCS[b]	1.6 ± 0.5	193 ± 29	0.41 ± 0.06	0.68 ± 0.14
Pt@NHCS$_{\Delta T}$[c]	3.2 ± 0.8	86 ± 13	0.35 ± 0.05	0.31 ± 0.07
Pt@HGS	<2	108 ± 10	0.41 ± 0.06	0.44 ± 0.09
Pt@HGS$_{\Delta T}$[c]	3.0 ± 0.8	75 ± 11	0.47 ± 0.07	0.35 ± 0.09
Pt/Vulcan	3.6 ± 0.7	67 ± 6	0.49 ± 0.06	0.32 ± 0.07

[a] All catalyst have a Pt loading of ca. 20 wt.%. [b] ECSA, SA, and MA determined at 0.9 V vs RHE in the anodic scan, after only 30 activation cycles in $HClO_4$ up to 1.35 V_{RHE} 0.2 V s^{-1}. [c] ECSA, SA, and MA determined after 300 activation cycles in $HClO_4$ up to 1.35 V_{RHE} 0.2 V s^{-1}.

The Pt nanoparticles were confined in the pore structure of NHCS as reported elsewhere.[45] Specifically, the initial Pt clusters were deposited by ultrasound-assisted incipient wetness impregnation and subsequent gas phase reduction with hydrogen. The high BET surface area of the NHCS support is beneficial to promote a high initial dispersion of the platinum precursor and Pt nanoparticles after the reduction process. Subsequently, a thermal treatment at 850 °C for 3 h under inert atmosphere is carried out to promote a controlled and mild growth of the platinum clusters inside the pore system—this process is referred to as pore confinement.[45] The as-made material prior to the thermal treatment step is denoted as Pt@NHCS, and the corresponding thermally treated material as Pt@NHCS$_{\Delta T}$. The X-ray powder diffraction pattern after thermal treatment at 850 °C (Figure S1B) presents the characteristic reflections of the face-centered cubic (fcc) Pt crystal structure. The NHCS support carbonized at 850 °C does not present macroscopically defined graphitic structure, but instead has a broad reflection at ca. 20° (2θ) associated with a turbostratic carbon structure (Figure S1B inset).

Representative high-resolution scanning electron micrographs (HR-SEM), dark field scanning transmission electron micrographs (DF-STEM), and DF-STEM images of cross-sectional cuttings of both materials, Pt@NHCS and Pt@NHCS$_{\Delta T}$, are shown in Figure 1. Figure 1A–C correspond to the as-made Pt@NHCS material, and Figure 1D–F shows the thermally treated material Pt@NHCS$_{\Delta T}$. Figure 1A,D are SEM micrographs that were imaged by both secondary electrons (SE) and high angle backscattered electrons (HA-BSE). It can be seen that the well-defined structure of the NHCS support is retained after the thermal treatment. The corresponding DF-STEM images (Figure 1B,E) allow the visualization of the high density and high dispersion of Pt nanoparticles throughout the whole mesopore system of the NHCS. The successful Pt pore confinement can be observed in the corresponding DF-STEM micrographs of the cross sections shown in Figure 1C,F. The Pt nanoparticles are uniformly distributed throughout the carbon shells before and after thermal treatment, being preferentially located within the porous shell. A minor fraction of Pt nanoparticles might be located at the inner or outer surface of the NHCS. Furthermore, the change in nanoparticle density, and therefore the average interparticle distance, upon thermal treatment is a consequence of the mild sintering of the Pt clusters during the pore confinement process.

The particle-size distributions before and after thermal treatment were determined by particle counting in DF-STEM micrographs. The measured particle-size distributions are based on the counting of particles that are large enough to be visualized by DF-STEM. Thus, smaller Pt clusters, possibly formed after the reduction process, are missed in the particle counting (see below). The visible Pt nanoparticles in the as-made material have a particle-size distribution centered at 1.6 ± 0.5 nm. After thermal treatment at 850 °C for 3 h, the Pt nanoparticles exhibited a homogeneous growth to 3.2 ± 0.8 nm. The corresponding particle-size distributions are shown in Figure S2.

After the reduction step and further thermal treatment to 850 °C, the evolution of the Pt and N surface chemical species was investigated by X-ray photoelectron spectroscopy (XPS). Figure 2 shows the N 1s and Pt 4f high resolution XPS spectra of Pt@NHCS and Pt@NHCS$_{\Delta T}$. All XPS binding energies were referenced to the graphitic C 1s signal of the carbon support at 284.5 (±0.1) eV.[72,75] The N 1s XPS spectra (Figure 2A,B) are predominantly composed of three nitrogen species: pyridinic (N-1), pyrrolic/pyridone (N-2), and quaternary (N-3) nitrogen species.[72,75] Additionally, pyridine-*N*-oxide (N-4) species can be found at higher binding energies with significantly lower intensities.[72,75] After the thermal treatment at 850 °C, which promotes the controlled particle pore confinement, the nitrogen content decreased from ca. 9 wt % to ca. 6 wt %. Furthermore, a slight change in the distribution of the nitrogen species is observed (Figure 2A,B). In particular, the ratio of the pyridinic nitrogen (N-1) to lower electron density nitrogen species (N-2 and N-3) is slightly lower after the thermal treatment. The Pt 4f XPS spectra of Pt@NHCS and Pt@NHCS$_{\Delta T}$ have in both cases defined peaks corresponding to metallic platinum, and the spectra contain no features associated with oxidized platinum species. The XPS binding energies, the surface elemental compositions, and the bulk elemental compositions of both NHCS-based materials are summarized in Table S1.

ORR Activity and Stability under Simulated Start–Stop Conditions. Electrochemical activity for the limiting ORR was investigated via RDE thin-film measurements following the experimental protocols reported in literature.[76,77] Figure S3 shows the background corrected positive scans of the ORR polarization curves at different rotation rates (400, 900, 1600, 2500 rpm; scan rate: 0.05 V s^{-1}, room temperature) and the corresponding Tafel plot (at 1600 rpm) of the as-made Pt@NHCS catalyst in 0.1 M $HClO_4$ saturated with oxygen. The corresponding thermally treated material Pt@NHCS$_{\Delta T}$ presents a comparable behavior if it is first subjected to an activation procedure, which is described in detail in the Experimental Section. This activation procedure consists of oxidizing electrochemically carbon residues deposited on the platinum nanoparticles during the thermal treatment carried out in the synthesis of the materials. Activities were calculated from the anodic scan of ORR polarization curves at 0.9 V_{RHE},

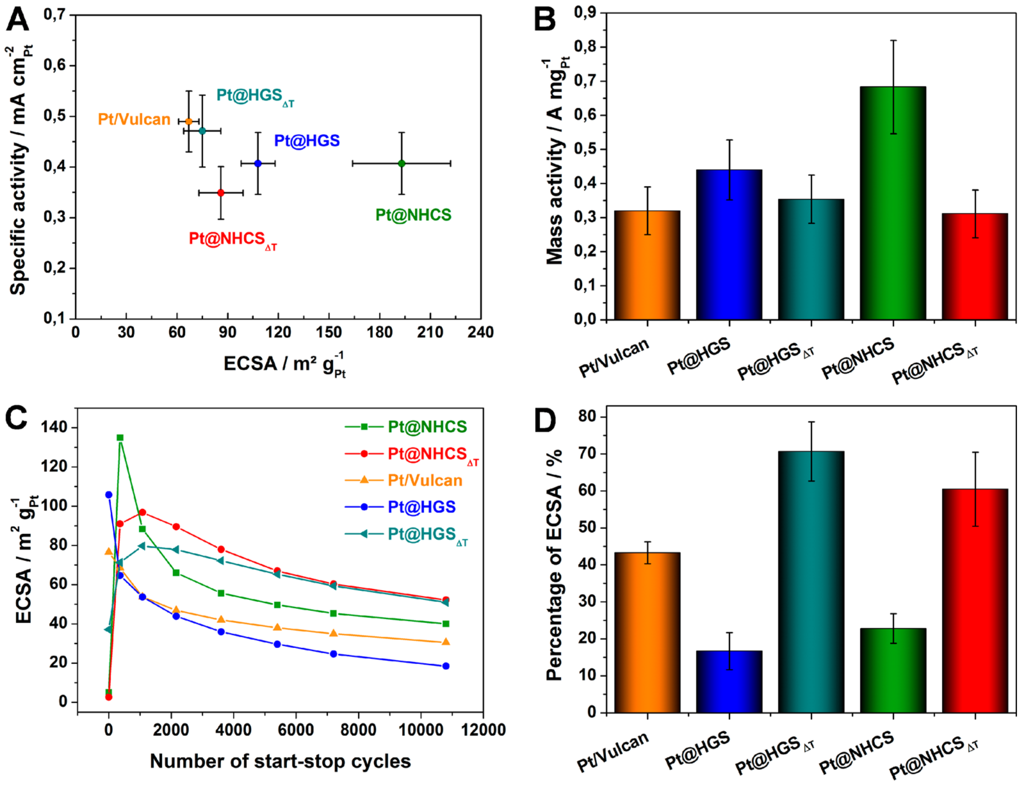

Figure 3. Comparison of the electrochemical properties of NHCS-, HGS-, and Vulcan-based electrocatalysts determined in 0.1 M $HClO_4$: (A) Specific activities at 0.9 V_{RHE} versus electrochemically active surface area; (B) corresponding mass activities; (C) comparison of ECSA change as monitored via CO-stripping during the ex situ accelerated degradation test (with a catalyst amount of 30 μg_{Pt} cm^{-2} at the working electrode) for each catalyst, with degradation cycles between 0.4 and 1.4 V_{RHE} at 1 V s^{-1}, the lines are only intended as a guide to the eye connecting points at which the ECSA was monitored; (D) comparison of remaining ECSA compared to ECSA (initial or after activation) in % after 10 800 degradation cycles.

scan rate of 0.05 V s^{-1} and at a rotation rate of 1600 rpm. Specific activity measurements at lower scan rates can be found in Figure S4 for comparison purposes. Table 1 summarizes the specific activities (i.e., kinetic current normalized to the platinum surface area), electrochemical surface areas (ECSA), and mass activities (i.e., kinetic current normalized to the mass of platinum). The NHCS-based materials are compared to a selection of three additional catalysts, which were previously investigated by us under the same conditions: a standard Pt/Vulcan[29] material and two analogous HGS-based[45,78] materials. All five materials have a platinum loading of approximately 20 wt % and can therefore be mainly distinguished on the basis of their particle size and type of support. A visualization of the data in Table 1 is provided in Figure 3A, which compares both specific activity and ECSA of the five materials. In general, both NHCS-based catalysts present specific activities as expected from their particle sizes, if compared with standard Pt/C catalysts.[78] This result indicates that this specific type of nitrogen-doped carbon does not promote any particular enhancement of the specific catalytic activity of platinum for ORR under the applied conditions.

The ECSA of the catalyst materials was determined by CO-stripping measurements following the methodologies described elsewhere.[79,80] The CO-stripping voltammograms of the as-made material Pt@NHCS and the corresponding thermal treated material are shown in Figure S5. The ECSA of nitrogen-doped materials is generally higher than for standard Pt/C catalysts. In particular, the as-made material Pt@NHCS has a remarkably high electrochemical surface area of 193 ± 29 m^2 g_{Pt}^{-1}, which is attributed to the small Pt cluster size. This ECSA would correspond to a theoretical particle size of ca. 1 nm, assuming that the particles are spherical and that 30% of the Pt surface is in contact with the carbon support, thus being not accessible for electrochemical reactions. Because the particle-size distributions suggest a higher particle size, one may thus conclude that small platinum clusters, with sizes that cannot be resolved with the microscope used, exist in this material.

Comparing the ECSAs of Pt@NHCS and the analogous not nitrogen-doped material Pt@HGS, the strong impact of nitrogen doping becomes evident. In particular, the ECSA of Pt@NHCS is almost twice as high as for Pt@HGS, besides the otherwise similar structural properties of both supports. This enhancement in ECSA is attributed to a significantly better dispersion in the NHCS, which has its origin likely in (i) the effect of nitrogen functionalities during platinum particle nucleation/growth, (ii) the higher BET surface area of the NHCS support (~1700 m^2 g^{-1}) compared to HGS (~1200 m^2 g^{-1}), and (iii) an improved wetting behavior of the nitrogen-doped carbon support during synthesis due to enhanced hydrophilicity of the support. Once the Pt@NHCS, with Pt particle size smaller than 2 nm, is thermally treated to 850 °C during the pore confinement process, the resulting Pt@NHCS$_{\Delta T}$ has similar specific activity as the analogous Pt@HGS with particle size of ca. 3–4 nm.[45] However, the slightly higher ECSA and the particle size from DF-TEM reveal a somewhat smaller average diameter of ca. 2–3 nm. This indicates that in the course of the thermal treatment at sufficiently high temperatures, not only will the size of the

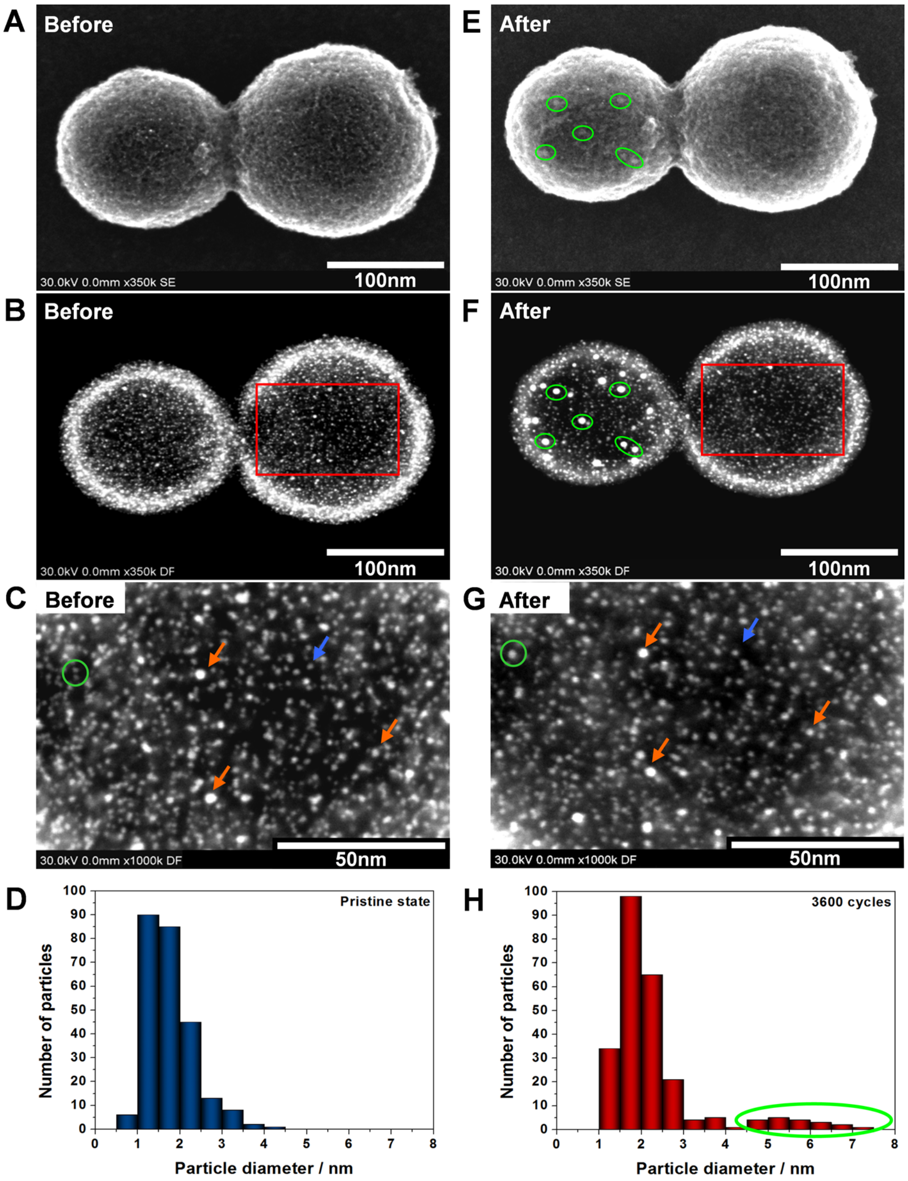

Figure 4. IL-SEM/DF-STEM micrographs of Pt@NHCS in the pristine state and after 3600 degradation cycles between 0.4 and 1.4 V_{RHE} at 1 V s^{-1} in $HClO_4$ and the corresponding particle-size distributions. (A,E) IL-SEM micrographs. (B,C,F,G) IL-DF-STEM where the higher magnification images correspond to the regions highlighted with the red squares. Orange arrows point at particles at identical locations, green circles draw attention to regions where particle growth is visible, and blue arrows point at particles that underwent dissolution. For the particle-size distribution determination ca. 250 nanoparticles were counted at several identical locations.

mesopores in which the particles are located have a dominant influence on the resulting particle size, but also the presence or absence of nitrogen-functionalities will have some effect as well.

The corresponding mass activities were calculated on the basis of the specific activity and ECSA. The values are depicted in the form of a bar plot in Figure 3B for better comparability. This graph highlights the major advantage of using Pt@NHCS as catalyst for ORR. The excellent dispersion and high ECSA result in a relatively high mass activity. This mass activity is about twice the activity of the other materials. This particular advantage is, however, lost after thermal treatment to 850 °C for the Pt@NHCS$_{\Delta T}$, which underwent a reduction of the ECSA, caused by the growth of Pt clusters inside the pore structure.

Highly dispersed Pt nanoparticles are intrinsically less stable due to the high surface energy associated with these systems. Therefore, extensive studies on the nitrogen-doped materials were performed in an electrochemical half-cell configuration in order to assess the influence of nitrogen-doping on material stability. Accelerated aging tests under simulated start–stop conditions (potential cycling between 0.4 and 1.4 V_{RHE} and scan rate of 1 V s^{-1}) were performed at room temperature in 0.1 M $HClO_4$ saturated with argon. All materials were tested under identical conditions, and the surface area change was monitored after 0, 360, 1080, 2160, 3600, 5400, 7200, and 10 800 potential cycles. Figure 3C shows representative measurements of the change in ECSA for the five catalyst materials. The behavior of Pt/Vulcan, Pt@HGS, and Pt@HGS$_{\Delta T}$ was already discussed in our previous works in more detail.[45,78] Particularly, Pt@HGS suffers from very drastic surface area losses, especially at the beginning of the degradation test, which was attributed to its small platinum particle size. However, the thermally treated

Pt@HGS$_{\Delta T}$ was demonstrated to be able to preserve a comparably high ECSA throughout the complete degradation test, with much smaller losses compared not only to the not thermally treated Pt@HGS but also to a standard Pt/Vulcan material of the same nanoparticle size and platinum loading. This was attributed to the pore confinement of platinum nanoparticles in the mesoporous structure of the support and was supported also by further experiments.[45]

Pt@NHCS and Pt@NHCS$_{\Delta T}$ catalysts have several similarities with the analogous HGS-based material. In particular, the shape of the curves reflecting the ECSA change during potential cycling at room temperature is remarkably similar to the shape of the corresponding nitrogen-free materials. Besides needing very few activation cycles (the maximum Pt@NHCS ECSA of ca. 193 $m^2\ g_{Pt}^{-1}$ is reached after only 30 cycles and after 360 cycles the ECSA decreases to ca. 140 $m^2\ g_{Pt}^{-1}$ as seen in the degradation test), the ECSA evolution curve of Pt@NHCS is almost parallel to the curve of the corresponding Pt@HGS material. However, the magnitude of ECSA is different for both materials: the ECSA is at any point significantly higher for Pt@NHCS compared to Pt@HGS. Overall, both nonthermally treated materials are characterized by a rather low stability considering the relative loss of ECSA compared to its initial value (or maximum value if activation cycles are necessary). This is visible in the bar plot in Figure 3D, which compares the remaining relative ECSA in % after 10 800 potential cycles for the five materials. For the two materials with initial particle sizes smaller than 2 nm, less than 30% of the original platinum surface area is retained. The excellent dispersion and small particle size, which is responsible for the high initial ECSAs and mass activities, are thus achieved at the expense of material stability. Nevertheless, it deserves to be mentioned that despite the higher relative ECSA loss of Pt@NHCS compared to Pt/Vulcan, its absolute ECSA does not fall at any point during the aggressive 10 800 cycles below the ECSA of Pt/Vulcan.

Both thermally treated materials, Pt@NHCS$_{\Delta T}$ with average particle size of about 2−3 nm and Pt@HGS$_{\Delta T}$ of about 3−4 nm, clearly show different ECSA decay behavior compared to the nonthermally treated materials. Namely, both materials first require several activation cycles so that it takes about 360 cycles until approximately 90% of the catalyst surface area is accessible. The significantly low ECSA values determined in the pristine state (0 cycles) of both thermally treated materials indicate the initial blockage of the platinum sites available for CO adsorption during the ECSA determination (Figure 3D). The ECSA increases with increasing the potential cycles, and the maximum in ECSA is reached after about 1000 potential cycles for both materials. The need for activation is attributed to the presence of carbon impurities on the platinum surface after the thermal treatment. Furthermore, some pores of the mesoporous support may be blocked as a consequence of particle sintering. The slightly higher maximum for the Pt@NHCS$_{\Delta T}$ system compared to Pt@HGS$_{\Delta T}$ is attributed to a slightly smaller platinum particle size, which may also be in part responsible for the somewhat steeper slope in ECSA decay after exceeding the maximum. The final ECSA after 10 800 potential cycles is, however, similar for both materials and the magnitude of the preserved ECSA at this point is significantly higher than for Pt/Vulcan. The relative loss for both thermally treated catalysts is appreciably smaller than for Pt/Vulcan, despite a comparable particle size. Thus, both materials offer improved stability under the applied potential cycling conditions at room temperature due to pore confinement; however, no obvious additional benefit can be identified for the nitrogen-doped material. The relative losses are in tendency even slightly higher for the nitrogen-doped material than for the nitrogen-free material. In this context, it is important to consider the slightly smaller particle sizes of the N-doped materials, which may explain the observed higher relative losses. In order to develop a better understanding about the underlying degradation mechanisms on the nanoscale for the nitrogen-doped materials, extensive IL-SEM/DF-STEM measurements will be discussed in the following section.

Investigation of the Degradation Processes on the Nanoscale. Identical location electron microscopy is a powerful tool for the investigation of the intrinsic electrochemical degradation mechanisms of electrocatalysts under well-defined ex situ conditions. In this work, IL-SEM/DF-STEM measurements were performed to explore the essential degradation mechanisms of the NHCS-based materials. Representative IL-SEM/DF-STEM micrographs of the as made Pt@NHCS material are shown in Figure 4. As the applied potential cycling conditions are very aggressive, 3600 cycles (instead of 10 800 cycles) were chosen to visualize the most important changes of the catalyst under such accelerated aging conditions. Particularly, in complex systems such as Pt@NHCS the most significant changes occur at the beginning of the catalyst lifetime during which the changes in ECSA are also most severe (see Figure 3). After 3600 degradation cycles, neither morphological changes nor changes in the topology of the NHCS surface are obvious in the IL-SEM micrographs (Figure 4A,E). DF-STEM analysis before electrochemical treatment visualizes the uniform and homogeneous distribution of Pt nanoparticles of ca. 1−2 nm in the NHCS shells (Figure 4B). As already mentioned, smaller Pt nanoparticles might also be present; however, it is not possible to clearly image them due to limitations in resolution. After 3600 start−stop degradation cycles, few Pt nanoparticles of significantly larger particle size, highlighted with green circles, are seen in Figure 4F. The large Pt nanoparticles are a clear sign of degradation via particle growth. From the SEM micrograph (Figure 4E), it is seen that the large particles are not located at the external surface of the spheres. In this SEM micrograph, the green circles draw attention to the positions where the large Pt nanoparticles are located. It is possible to see low intensity spots that appear brighter than the carbon phase. These brighter spots correspond to the Pt nanoparticles, which can be detected due to backscattered electrons from the bulk of the sample. Thus, the large Pt nanoparticles can either be located at the other side of the sphere, inside the spheres, or inside the shells.

Figure 4C,G show more details of the IL-DF-STEM micrographs. The high-magnification images correspond to the regions highlighted with red squares in Figure 4B,F. A first look at the images recorded at higher magnification does not reveal a severe loss of Pt nanoparticles; in fact, the number of visualized particles is retained to a remarkable extent after the 3600 degradation cycles. From the macroscopic electrochemical stability investigations (Figure 3D), Pt@NHCS suffers from a significant loss of platinum electrochemical surface area during the first 3600 degradation cycles. However, from the IL-DF-STEM measurements shown in Figure 4G, this loss of platinum surface area cannot easily be recognized, because the number of visualized particles and the average particle size change only slightly after 3600 degradation cycles. One possible explanation

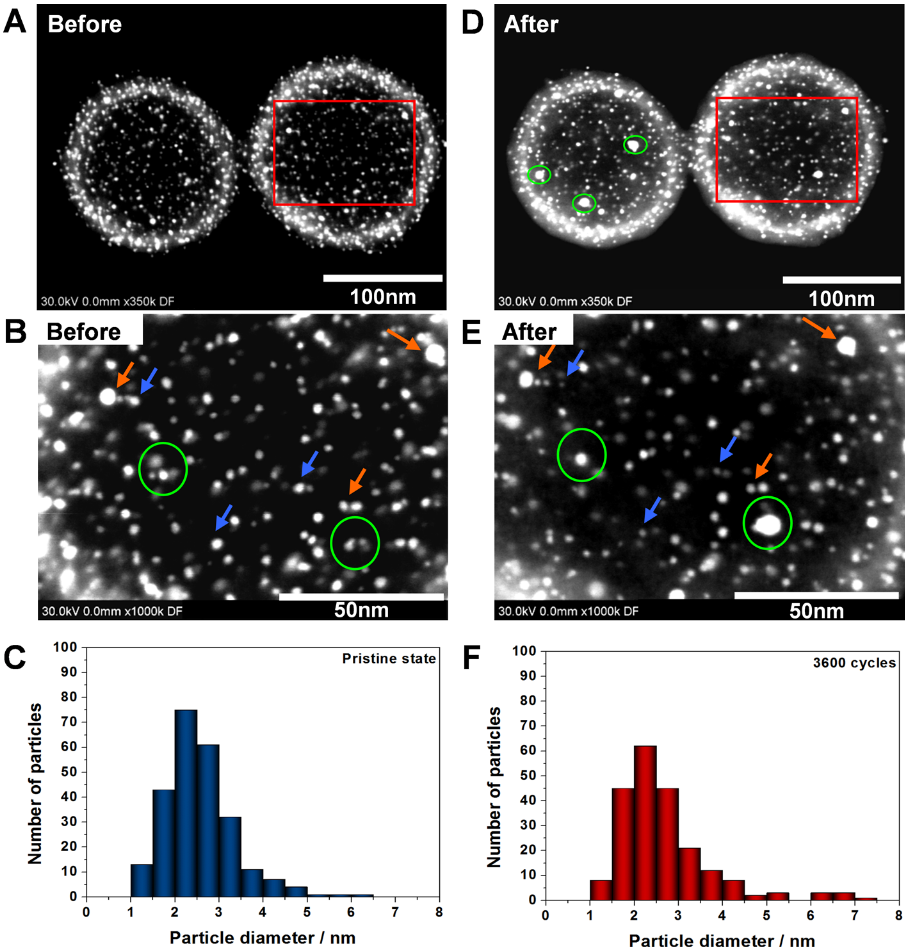

Figure 5. IL-DF-STEM micrographs of Pt@NHCS$_{\Delta T}$ in the pristine state and after 3600 degradation cycles with the corresponding particle-size distributions. Higher-magnification images (B,E) correspond to the regions highlighted with the red squares. Orange arrows point at particles at identical locations, green circles draw attention to regions where particle growth is visible, and blue arrows point at particles that underwent dissolution. For the particle-size distribution determination, ca. 250 nanoparticles were counted at several identical locations.

for this observation might be that the initial loss of platinum surface area in the macroscopic electrochemical stability investigations corresponds to the dissolution of subnanometer sized platinum clusters, which cannot be clearly visualized in the IL-DF-STEM. Dissolution has been proposed to be a dominant degradation mechanism in Pt-based catalysts with nanoparticles smaller than 2 nm.[24,78,81] Furthermore, similar potential cycling protocols were recently demonstrated to cause detectable dissolution even for bulk platinum.[82] After the dissolution of the subnanometer sized platinum clusters, the further degradation is proceeding slower compared to the initial losses as evident from Figure 3C; however, it does not completely stop.

Figure 4D,H show the particle-size distributions before and after 3600 degradation cycles. Before the electrochemical degradation treatment, the particle-size distribution of the detected Pt nanoparticles is centered at around 1.5 nm. After 3600 degradation cycles, a bimodal particle-size distribution is observed. The initial distribution is centered at ca. 1.5 nm, and a new broad distribution at larger particle diameters of ca. 4 to 8 nm appears, associated with the aforementioned particle growth processes. The bimodal particle-size distribution and the formation of large platinum particles (as seen in Figure 4F) suggest that Ostwald ripening (i.e., the dissolution of smaller particles and successive redeposition of platinum on larger particles) might be a potential cause for the observed particle growth. In general, Ostwald ripening is considered as less probable to be observed via IL-TEM[30] than in real fuel cells. Similar to IL-TEM measurements, no extended 3D catalyst layer is present and the catalyst is subjected to a large volume of electrolyte, and therefore, the concentration of dissolved platinum species at the catalyst/electrolyte interface can be expected to be very small. However, if strong dissolution takes place in a short period of time, high concentrations of platinum species may be reached at the catalyst/electrolyte interface. This might in particular be possible for catalysts with small particle sizes and high ECSA. The ECSA of Pt@NHCS is very high and thus particle growth due to redeposition of platinum appears feasible.

The second possible cause for particle growth is agglomeration and coalescence of particles in proximity to each other. Sintering of platinum particles during the pore confinement already indicates that many particles in the pristine Pt@NHCS material are in sufficient proximity to each other and that the interparticle distances are thus not too large for agglomeration or coalescence to occur. However, upon the electrochemical degradation, the size of the final larger platinum nanoparticles, 4–8 nm, exceed the size of the average pore diameter of the mesopores in the NHCS (i.e., < 4 nm), which indicates that other mechanisms involving changes in the NHCS pore structure might play a role.

Carbon corrosion is considered a primary degradation mechanism, which can facilitate secondary degradation processes such as platinum particle detachment or agglomeration, due to a weakening of the bonding between platinum particle and carbon support at the interface. Carbon corrosion, even if macroscopically not visible, is very likely to occur at the Pt/C interface due to the catalytic activity of platinum for carbon oxidation. As carbon corrosion depends significantly on the local properties of the carbon, heterogeneity in the particle growth processes (Figure 4F) could also be tentatively attributed to heterogeneities of the carbon support. In particular, synthesis procedures involving carbonization steps at high temperatures are known to result in carbon materials, where carbon properties (surface functionalities, degree of graphitization, porosity, etc.) are rarely perfectly homogeneous throughout the complete system. In this case, agglomeration as a secondary degradation mechanism, caused by the primary carbon corrosion process, might be a possible cause of the observed particle growth. In this case, heterogeneities of the carbon support can generate different local corrosion profiles generating heterogeneous particle growth, as observed in Figure 4F. Thus, the significant particle growth would occur particularly at regions where carbon corrosion takes places. In contrast, in the places where carbon corrosion does not play a significant role, the particles are effectively stabilized by the textural properties of the NHCS support.

After the thermal treatment at 850 °C, the thermally induced sintering of the initial Pt clusters results in Pt nanoparticles of around 2−3 nm inside the pore structure of the NHCS support. Figure 5 presents IL-DF-STEM micrographs and the corresponding particle-size distributions before and after 3600 degradation cycles. The larger Pt particle size in this case is obvious when comparing with the predecessor Pt@NHCS material. The overall change of the material after electrochemical degradation is minor, which is in good agreement with the thin-film measurements (Figure 3C). A few larger nanoparticles are also observed in this material but to a much lesser extent than in the case of Pt@NHCS. In general, the density of particles and the size of most of the visible particles did not change significantly. However, for some particles, indications of particle growth and dissolution can be observed. To follow the most important changes, the orange arrows point at Pt nanoparticles that did not suffer significant changes, helping to identify the identical locations throughout the images. Particle growth can be observed in the locations highlighted with the green circles. In the IL-DF-STEM micrographs of the material before electrochemical treatment, several Pt nanoparticles are distinguishable in the green circles. Instead, after 3600 degradation cycles, only one large Pt nanoparticle is visible at the same location. The nature of the mild particle growth in this case is not clear. It might be associated with particle migration with agglomeration of small Pt clusters located in the same pores or upon local carbon corrosion. The particle-size distribution in this case does not change after electrochemical degradation, demonstrating that particle growth processes are minor. Furthermore, a detailed inspection of the IL-DF-STEM micrographs gives clear indications of dissolution processes. Particularly, some small residual Pt nanoparticles can be found after the degradation treatment, and some Pt particles have completely vanished. For instance, the Pt nanoparticles pointed at with the blue arrows clearly show a decrease in particle size after the 3600 degradation cycles.

In summary, the properties of the NHCS support have been proven to be very beneficial to promote a high dispersion of Pt nanoparticles. In addition, for the as-made material Pt@NHCS, the unique properties of the NHCS support provide excellent conditions for a good separation of the small platinum clusters, resulting in a very high mass activity. However, such high mass activity could not be retained over an extended period due to the relatively low stability of this material under the applied conditions. On the other hand, for the thermally treated material Pt@NHCS$_{\Delta T}$, catalyst activities were not significantly changed compared to the nitrogen-free support, but the successful pore confinement of the Pt nanoparticles resulted in a remarkable electrochemical stabilization, comparable to the analogous HGS-based material. In both cases, the degradation mechanisms observed via identical location electron microscopy are slightly different than for the analogous HGS-based materials. In particular, particle growth is found to play a major role for the Pt@NHCS compared to Pt@HGS. Pt@NHCS$_{\Delta T}$ showed some minor particle growth as well, which had been completely suppressed for Pt@HGS$_{\Delta T}$. Remarkable is the observation of heterogeneous particle growth for the NHCS-based materials. This behavior is tentatively attributed to local carbon corrosion occurring as primary degradation process, and promoting the particle growth is assigned as secondary degradation process. As carbon corrosion at the platinum carbon interface can be expected to play a role under the applied aggressive potential cycling conditions, the heterogeneous particle growth behavior can be tentatively attributed to local heterogeneities in the carbon support. In this case, a higher susceptibility of the NHCS material toward carbon corrosion under highly oxidative conditions might help to explain the more pronounced particle growth. Stronger carbon corrosion for the NHCS materials compared to HGS is not surprising due to the improved graphitization degree of the latter, which is known to reduce carbon corrosion. Thus, the observations for our model system indicate that nitrogen doping is indeed beneficial for promoting highly dispersed nanoparticle-based catalyst, but it does not always lead to significant benefits regarding material stability, as frequently claimed in the literature.

■ CONCLUSIONS

The electrochemical investigations demonstrated the suitability of NHCS derived from carbonization of polyacrylonitrile at 850 °C as a catalyst support for low temperature fuel cells. The nitrogen functionalities promote an enhancement of Pt electrochemical surface area, resulting in electrocatalysts with high initial mass activities. The specific activity of Pt nanoparticles supported in NHCS was, however, comparable to an analogous Pt/C catalyst of comparable platinum particle size. Therefore, it is concluded that this type of nitrogen-doped carbon does not promote any enhancement of the Pt specific activity in the ORR in acidic electrolytes. The electrochemical stability of the NHCS-based catalysts was studied under ex situ conditions simulating the detrimental start−stop conditions of a fuel cell under operation. It was found that the overall retention of Pt electrochemical surface area of Pt@NHCS$_{\Delta T}$ is higher compared to standard Pt/Vulcan. However, the as-made material Pt@NHCS exhibited higher percentage losses of ECSA, particularly at the beginning of its lifetime. The thermally treated material Pt@NHCS$_{\Delta T}$ showed higher electrochemical stability due to the confined nature of the Pt nanoparticles and due to the larger particle size. The macroscopic electrochemical behavior of both NHCS-based materials was in most aspects comparable to the analogous HGS-based materials. The investigation of the underlying degradation mechanisms occurring in the NHCS-based materials was investigated by IL-SEM/DF-STEM measurements. The as-made material Pt@NHCS did not show a strong loss in total number of particles of ca. 1−2 nm after 3600 degradation cycles. The initial loss of Pt surface area was thus tentatively attributed to be associated with the dissolution of unstable subnanometer sized Pt clusters. Furthermore, this material also suffered from some particle growth processes. These particle growth processes are tentatively ascribed to occur as consequence of agglomeration, occurring as a result of local carbon corrosion. Furthermore, Ostwald ripening type degradation processes appear plausible for such systems that are susceptible to strong platinum dissolution. In the case of the thermally treated material, the degradation processes were found to be not as pronounced. However, particle growth and dissolution processes were also observed to a minor extent, while particle growth was completely suppressed for the analogous Pt@HGS$_{\Delta T}$ material. Overall, nitrogen-doping can offer benefits for achieving high initial mass activities due to the high platinum dispersion, but it was not found to be of advantage with respect to material stability.

■ EXPERIMENTAL SECTION

Synthesis and Characterization of the Materials. Polyacrylonitrile (PAN)-based nitrogen-doped hollow carbon spheres (NHCS) were synthesized following the procedure developed by Lu et al.[60] with the modification of the silica exotemplate, the synthesis of which is described in detail in the Supporting Information. A typical synthesis route for NHCS is as follows: 1 g of the silica exotemplate material (with a total pore volume of ca. 0.35 cm^3 g^{-1} determined by N_2 physisorption) is evacuated under vacuum for 1 h. Afterward, a mixture of 0.35 mL acrylonitrile (ACN) and 3 mg of azobis(isobutyronitrile) (AIBN) is incorporated into the mesopores of the silica exotemplate via the incipient-wetness method under Ar. The resulting material is transferred to a steel autoclave and heated to 50 °C for 12 h, followed by additional 8 h at 60 °C. In these thermal steps, a PAN homopolymer is synthesized by a conventional radical polymerization. Afterward, the polymer composite is heated to 200 °C for 18 h under air in order to stabilize the homopolymer and to increase the carbon yield. The carbonization of PAN in the mesopores of the silica exotemplate is achieved by thermal treatment to 850 °C (heating rate of 5 °C min^{-1}) for 4 h under nitrogen flow. The silica exotemplate is dissolved by using an aqueous HF (10 vol %) solution for 6 h. The material is then washed four times with distilled water and once with ethanol. The washing process is carried out by centrifugation (14 000 rpm, 5 min) and redispersion assisted by ultrasonication (5 min). Finally, the material is dried at 75 °C overnight. Thermogravimetric analysis showed that the silica content in the product was <1%.

Pt nanoparticles supported on NHCS (20 wt %) were synthesized via ultrasound assisted impregnation of $H_2PtCl_6 \cdot xH_2O$ solution in ethanol and further gas phase reduction under H_2/Ar atmosphere, as reported elsewhere.[45] Typically, the exact amount of $H_2PtCl_6 \cdot xH_2O$ precursor corresponding to a theoretical 20 wt % of Pt content in the final material is dissolved in a volume of ethanol equivalent to the pore volume of the NHCS (measured by N_2 physisorption). For 100 mg of NHCS, 66 mg of $H_2PtCl_6 \cdot xH_2O$ are dissolved in ca. 0.14 mL of ethanol. The resulting solution is impregnated onto the NHCS support, and the slurry is further ultrasonicated for 30 min. Subsequently, the ethanol is evaporated under Ar flow at 100 °C during 1 h in a glass tube furnace. Afterwards, the reduction step is carried out in the same glass tube furnace using a mixture of H_2 30 vol % in Ar. The sample is then heated to 250 °C with a rate of 2.5 °C/min and kept at this temperature for 3 h. After the reduction is finished, the H_2 flow is turn off, and the material is high temperature annealed under Ar. Pt@NHCS were treated at 850 °C under Ar for 3 h. Details on the instruments utilized for the characterization of the materials can be found in the Supporting Information.

Ex Situ Half-Cell Electrochemical Measurements. The catalyst powders are dispersed ultrasonically in ultrapure water (18 MΩ, Millipore) for at least 30 min initially and again for at least 10 min prior to pipetting onto the glassy carbon discs (5 mm diameter, 0.196 cm^2 geometrical surface area). The catalyst suspensions are dried in air or under mild vacuum. The electrochemical setup consists of a three-electrode, three-compartment cell, completely made from Teflon. A rotating disc electrode (RDE) functions as working electrode. A graphite rod is used as counter electrode, whereas an Ag/AgCl electrode (Methrom), housed in a separate compartment, functions as reference electrode. The reference electrode compartment is separated from the main compartment with a Nafion membrane to avoid contamination with chlorides during activity and stability tests. The Gamry Reference 600 potentiostat, a Radiometer Analytical rotation controller as well as a self-made gas purge system are all automatically regulated employing an in-house developed LabVIEW software.[83] All potentials are given with respect to the reversible hydrogen electrode potential (RHE), which is experimentally determined for each measurement. Both activity and stability measurements are performed in 0.1 M $HClO_4$ at room temperature. The electrolyte is prepared with ultrapure water and concentrated $HClO_4$ (Merck, Suprapur). Solution resistance is compensated for in all electrochemical measurements via positive feedback so that the residual uncompensated resistance is smaller than 4Ω. Activity measurements are performed for different amounts of catalyst for each material at the working electrode. Loadings are in the range of 5 to 30 μg_{Pt} cm^{-2} in order to obtain thin and well-dispersed catalyst films. In the case of the activity determination the catalyst materials are subjected to activation cycles before activity measurements until a stable cyclovoltammogram is obtained. This procedure is extended for the Pt@NHCS$_{\Delta T}$ catalyst to several hundred (typically 300) activation cycles between 0.05−1.35 V_{RHE} at scan rate of 0.2 V s^{-1} for removal of carbon impurities, prior to determination of SA and ECSA. The general guidelines for activity measurements are followed as described previously.[76,77] Specific activities are calculated from the positive scan of RDE polarization curves at 0.9 V_{RHE}, a rotation rate of 1600 rpm and a scan rate of 0.05 V s^{-1}. In order to isolate current related to oxygen reduction, the RDE polarization curves are corrected for capacitive processes. For this purpose, a cyclovoltammogram recorded with the same scan rate and potential window but in argon-saturated solution is subtracted from the ORR polarization curves. The platinum surface area of the catalyst is studied via CO stripping. In each CO-stripping experiment, carbon monoxide is adsorbed on the catalyst in a potential region (e.g., 0.05 V_{RHE}) at which no CO oxidation occurs, until the saturation coverage is reached. Afterward all remaining carbon monoxide is removed from the electrolyte by purging with argon, whereas the potential is held constant at the same value. Finally, CO is oxidized electrochemically to CO_2, and the charge corresponding to the CO oxidation is measured by the area of the oxidation peak. A more detailed description of general features of CO-stripping measurements can be found in the literature.[29,79,80] The mass activity is calculated based on the specific activity and electrochemical active surface area (ECSA), which is determined independently with several CO-stripping experiments for different catalyst loadings at the working electrode. The electrochemical degradation tests consist of 10 800 potential cycles (triangular wave) between 0.4 and 1.4 V_{RHE} with a sweep rate of 1 V s^{-1} without rotation. In this case, no extra cleaning of the catalyst is performed before starting the degradation to follow the changes in platinum surface area from the beginning. CO stripping is applied to monitor the real platinum surface area after 0, 360, 1080, 2160, 3600, 5400, 7200, and 10 800 potential cycles. The aging tests for all materials were performed with an identical amount of catalyst (i.e., mass of platinum) at the working electrode, namely, 30 μg_{Pt} cm^{-2}.

IL-SEM/DF-STEM Measurements. The catalyst suspensions of Pt@NHCS and Pt@NHCS$_{\Delta T}$ for the stability tests are diluted by a factor of about 1:5 with ultrapure water. Five microliters of the diluted suspension is loaded at the top side of a gold finder grid (NHA7, Plano) coated with a carbon film (Quantifoil R2/2). To avoid high catalyst loadings, which can result in overlapping catalyst particles, the drop is absorbed off the grid with a tissue after a few seconds. The grid is dried and images are recorded with the Hitachi S-5500 ultrahigh-resolution cold field emission scanning electron microscope at 30 kV. The electrochemical cell employed above for half-cell measurements is also utilized for the IL-SEM/STEM tests along with a comparable electrochemical protocol. A total of 3600 degradation cycles between 0.4 and 1.4 V_{RHE} with a sweep rate of 1 V s^{-1} without rotation is applied in with argon saturated 0.1 M $HClO_4$. Positive feedback IR compensation is performed accordingly. The catalyst deposited on the TEM grid is treated electrochemically by immobilizing the gold finder grid on the glassy carbon disc working electrode with the help of a Teflon cap as reported previously.[29] Micrographs of identical catalyst locations are taken after 0 and after 3600 degradation cycles. Further information regarding the basic IL-TEM method can be found in the literature.[29,30,84,85]

■ ASSOCIATED CONTENT

Ⓢ Supporting Information

The following additional information is reported in the Supporting Information: synthesis of the silica exotemplate, description of characterization methods, nitrogen adsorption isotherms, X-ray diffraction patterns, ORR polarization curves, Tafel plots, and CO-stripping curves. This material is available free of charge via the Internet at http://pubs.acs.org.

■ AUTHOR INFORMATION

Corresponding Authors

*E-mail: dcgaleanon@icloud.com. Phone: (+49) 1525 6458467 (C. G.).
*E-mail: schueth@mpi-muelheim.mpg.de. Fax: (+49) 208-306-2995 (F. S.).

Author Contributions

§C.G. and J.C.M. contributed equally.

Notes

The authors declare no competing financial interest.

■ ACKNOWLEDGMENTS

We thank Dr. Claudia Weidenthaler for the XPS measurements at MPI für Kohlenforschung. We are also grateful to Dr. Volker Peinecke and Dr. Ivan Radev from the fuel cell research center ZBT GmbH for the scientific discussions. J.C.M. acknowledges financial support by the Kekulé Fellowship from the Fonds der Chemischen Industrie (FCI), and F.S. acknowledges financial support by the DFG within the DFG-AIF-Cluster "MT-PEM".

■ REFERENCES

(1) Schlögl, R. *ChemSusChem* **2010**, *3*, 209−222.
(2) Gasteiger, H. A.; Kocha, S. S.; Sompalli, B.; Wagner, F. T. *Appl. Catal., B* **2005**, *56*, 9−35.
(3) Gasteiger, H. A.; Marković, N. M. *Science* **2009**, *324*, 48−49.
(4) Rabis, A.; Rodriguez, P.; Schmidt, T. J. *ACS Catal.* **2012**, *2*, 864−890.
(5) Greeley, J.; Stephens, I. E. L.; Bondarenko, A. S.; Johansson, T. P.; Hansen, H. A.; Jaramillo, T. F.; Rossmeisl, J.; Chorkendorff, I.; Nørskov, J. K. *Nat. Chem.* **2009**, *1*, 552−556.
(6) Hasché, F.; Oezaslan, M.; Strasser, P. *ChemCatChem* **2011**, *3*, 1805−1813.
(7) Hasché, F.; Oezaslan, M.; Strasser, P. *J. Electrochem. Soc.* **2012**, *159*, B24−B33.
(8) Lima, A.; Coutanceau, C.; LÉger, J. M.; Lamy, C. *J. Appl. Electrochem.* **2001**, *31*, 379−386.
(9) Mani, P.; Srivastava, R.; Strasser, P. *J. Phys. Chem. C* **2008**, *112*, 2770−2778.
(10) Mani, P.; Srivastava, R.; Strasser, P. *J. Power Sources* **2011**, *196*, 666−673.
(11) Marković, N. M.; Schmidt, T. J.; Stamenković, V.; Ross, P. N. *Fuel Cells* **2001**, *1*, 105−116.
(12) Oezaslan, M.; Strasser, P. *J. Power Sources* **2011**, *196*, 5240−5249.
(13) Stamenkovic, V. R.; Mun, B. S.; Mayrhofer, K. J. J.; Ross, P. N.; Markovic, N. M. *J. Am. Chem. Soc.* **2006**, *128*, 8813−8819.
(14) Strasser, P.; Koh, S.; Anniyev, T.; Greeley, J.; More, K.; Yu, C.; Liu, Z.; Kaya, S.; Nordlund, D.; Ogasawara, H.; Toney, M. F.; Nilsson, A. *Nat. Chem.* **2010**, *2*, 454−460.
(15) Strasser, P.; Koh, S.; Greeley, J. *Phys. Chem. Chem. Phys.* **2008**, *10*, 3670−3683.
(16) Wang, C.; Marković, N. M.; Stamenkovic, V. R. *ACS Catal.* **2012**, *2*, 891−898.
(17) Zhong, C.-J.; Luo, J.; Njoki, P. N.; Mott, D.; Wanjala, B.; Loukrakpam, R.; Lim, S.; Wang, L.; Fang, B.; Xu, Z. *Energy Environ. Sci.* **2008**, *1*, 454−466.
(18) Borup, R.; Meyers, J.; Pivovar, B.; Kim, Y. S.; Mukundan, R.; Garland, N.; Myers, D.; Wilson, M.; Garzon, F.; Wood, D.; Zelenay, P.; More, K.; Stroh, K.; Zawodzinski, T.; Boncella, J.; McGrath, J. E.; Inaba, M.; Miyatake, K.; Hori, M.; Ota, K.; Ogumi, Z.; Miyata, S.; Nishikata, A.; Siroma, Z.; Uchimoto, Y.; Yasuda, K.; Kimijima, K.-i.; Iwashita, N. *Chem. Rev.* **2007**, *107*, 3904−3951.
(19) Meyers, J. P.; Darling, R. M. *J. Electrochem. Soc.* **2006**, *153*, A1432−A1442.
(20) Knights, S. D.; Colbow, K. M.; St-Pierre, J.; Wilkinson, D. P. *J. Power Sources* **2004**, *127*, 127−134.
(21) Gasteiger, H. A.; Garche, J. In *Handbook of Heterogeneous Catalysis*; Wiley-VCH Verlag GmbH & Co. KGaA: Weinheim, 2008.
(22) Kinoshita, K.; Lundquist, J. T.; Stonehart, P. *J. Electroanal. Chem. Interfacial Electrochem.* **1973**, *48*, 157−166.
(23) Yu, P. T.; Gu, W.; Makharia, R.; Wagner, F. T.; Gasteiger, H. A. *ECS Trans.* **2006**, *3*, 797−809.

(24) Shao-Horn, Y.; Sheng, W.; Chen, S.; Ferreira, P.; Holby, E.; Morgan, D. *Top. Catal.* **2007**, *46*, 285−305.

(25) Shao-Horn, Y.; Ferreira, P.; la O', G. J.; Morgan, D.; Gasteiger, H. A.; Makharia, R. *ECS Trans.* **2006**, *1*, 185−195.

(26) Tang, H.; Qi, Z.; Ramani, M.; Elter, J. F. *J. Power Sources* **2006**, *158*, 1306−1312.

(27) Hartnig, C.; Schmidt, T. J. *J. Power Sources* **2011**, *196*, 5564−5572.

(28) Reiser, C. A.; Bregoli, L.; Patterson, T. W.; Yi, J. S.; Yang, J. D.; Perry, M. L.; Jarvi, T. D. *Electrochem. Solid-State Lett.* **2005**, *8*, A273−A276.

(29) Meier, J. C.; Galeano, C.; Katsounaros, I.; Topalov, A. A.; Kostka, A.; Schüth, F.; Mayrhofer, K. J. J. *ACS Catal.* **2012**, *2*, 832−843.

(30) Meier, J. C.; Katsounaros, I.; Galeano, C.; Bongard, H. J.; Topalov, A. A.; Kostka, A.; Karschin, A.; Schüth, F.; Mayrhofer, K. J. J. *Energy Environ. Sci.* **2012**, *5*, 9319−9330.

(31) Sun, X.; Saha, M. S. In *PEM Fuel Cell Electrocatalysts and Catalyst Layers*; Zhang, J., Ed.; Springer: London, 2008; p 655.

(32) Li, L.; Xing, Y. *J. Phys. Chem. C* **2007**, *111*, 2803−2808.

(33) Kruusenberg, I.; Alexeyeva, N.; Tammeveski, K.; Kozlova, J.; Matisen, L.; Sammelselg, V.; Solla-Gullón, J.; Feliu, J. M. *Carbon* **2011**, *49*, 4031−4039.

(34) Li, X.; Hsing, I. M. *Electrochim. Acta* **2006**, *51*, 5250−5258.

(35) Orfanidi, A.; Daletou, M. K.; Neophytides, S. G. *Appl. Catal., B* **2011**, *106*, 379−389.

(36) Hasche, F.; Oezaslan, M.; Strasser, P. *Phys. Chem. Chem. Phys.* **2010**, *12*, 15251−15258.

(37) Yu, P.; Gu, W.; Zhang, J.; Makharia, R.; Wagner, F.; Gasteiger, H. In *Polymer Electrolyte Fuel Cell Durability*; Büchi, F., Inaba, M., Schmidt, T., Eds.; Springer: New York, 2009; p 29.

(38) Stevens, D. A.; Hicks, M. T.; Haugen, G. M.; Dahn, J. R. *J. Electrochem. Soc.* **2005**, *152*, A2309−A2315.

(39) Selvaganesh, S. V.; Sridhar, P.; Pitchumani, S.; Shukla, A. K. *J. Electrochem. Soc.* **2013**, *160*, F49−F59.

(40) Kibsgaard, J.; Gorlin, Y.; Chen, Z.; Jaramillo, T. F. *J. Am. Chem. Soc.* **2012**, *134*, 7758−7765.

(41) Debe, M. K.; Schmoeckel, A.; Hendricks, S.; Vernstrom, G.; Haugen, G.; Atanasoski, R. *ECS Trans.* **2006**, *1*, 51−56.

(42) Debe, M. K.; Schmoeckel, A. K.; Vernstrom, G. D.; Atanasoski, R. *J. Power Sources* **2006**, *161*, 1002−1011.

(43) Bonakdarpour, A.; Stevens, K.; Vernstrom, G. D.; Atanasoski, R.; Schmoeckel, A. K.; Debe, M. K.; Dahn, J. R. *Electrochim. Acta* **2007**, *53*, 688−694.

(44) Debe, M. K.; Steinbach, A. J.; Vernstrom, G. D.; Hendricks, S. M.; Kurkowski, M. J.; Atanasoski, R. T.; Kadera, P.; Stevens, D. A.; Sanderson, R. J.; Marvel, E.; Dahn, J. R. *J. Electrochem. Soc.* **2011**, *158*, B910−B918.

(45) Galeano, C.; Meier, J. C.; Peinecke, V.; Bongard, H.; Katsounaros, I.; Topalov, A. A.; Lu, A.; Mayrhofer, K. J. J.; Schüth, F. *J. Am. Chem. Soc.* **2012**, *134*, 20457−20465.

(46) Qu, L.; Liu, Y.; Baek, J.-B.; Dai, L. *ACS Nano* **2010**, *4*, 1321−1326.

(47) Wang, H.; Maiyalagan, T.; Wang, X. *ACS Catal.* **2012**, *2*, 781−794.

(48) Zhang, L.; Xia, Z. *J. Phys. Chem. C* **2011**, *115*, 11170−11176.

(49) Lee, K. R.; Lee, K. U.; Lee, J. W.; Ahn, B. T.; Woo, S. I. *Electrochem. Commun.* **2010**, *12*, 1052−1055.

(50) Hasché, F.; Fellinger, T.-P.; Oezaslan, M.; Paraknowitsch, J. P.; Antonietti, M.; Strasser, P. *ChemCatChem* **2012**, *4*, 479−483.

(51) Liu, R.; Wu, D.; Feng, X.; Muellen, K. *Angew. Chem., Int. Ed.* **2010**, *49*, 2565−2569.

(52) Yang, W.; Fellinger, T.-P.; Antonietti, M. *J. Am. Chem. Soc.* **2010**, *133*, 206−209.

(53) Guo, Y.; He, J.; Wang, T.; Xue, H.; Hu, Y.; Li, G.; Tang, J.; Sun, X. *J. Power Sources* **2011**, *196*, 9299−9307.

(54) Ayala, P.; Arenal, R.; Rümmeli, M.; Rubio, A.; Pichler, T. *Carbon* **2010**, *48*, 575−586.

(55) Sun, C.-L.; Chen, L.-C.; Su, M.-C.; Hong, L.-S.; Chyan, O.; Hsu, C.-Y.; Chen, K.-H.; Chang, T.-F.; Chang, L. *Chem. Mater.* **2005**, *17*, 3749−3753.

(56) Vijayaraghavan, G.; Stevenson, K. J. *Langmuir* **2007**, *23*, 5279−5282.

(57) Zhou, Y.; Neyerlin, K.; Olson, T. S.; Pylypenko, S.; Bult, J.; Dinh, H. N.; Gennett, T.; Shao, Z.; O'Hayre, R. *Energy Environ. Sci.* **2010**, *3*, 1437−1446.

(58) Zhou, Y.; Pasquarelli, R.; Holme, T.; Berry, J.; Ginley, D.; O'Hayre, R. *J. Mater. Chem.* **2009**, *19*, 7830−7838.

(59) Shao, Y.; Sui, J.; Yin, G.; Gao, Y. *Appl. Catal., B* **2008**, *79*, 89−99.

(60) Lu, A.; Kiefer, A.; Schmidt, W.; Schüth, F. *Chem. Mater.* **2003**, *16*, 100−103.

(61) Maldonado, S.; Stevenson, K. J. *J. Phys. Chem. B* **2004**, *108*, 11375−11383.

(62) Ye, S.; Vijh, A. K.; Dao, L. H. *J. Electrochem. Soc.* **1997**, *144*, 90−95.

(63) Su, F.; Zhao, X. S.; Wang, Y.; Wang, L.; Lee, J. Y. *J. Mater. Chem.* **2006**, *16*, 4413−4419.

(64) Chen, H.; Yang, Y.; Hu, Z.; Huo, K.; Ma, Y.; Chen, Y.; Wang, X.; Lu, Y. *J. Phys. Chem. B* **2006**, *110*, 16422−16427.

(65) Chen, L. C.; Wen, C. Y.; Liang, C. H.; Hong, W. K.; Chen, K. J.; Cheng, H. C.; Shen, C. S.; Wu, C. T.; Chen, K. H. *Adv. Funct. Mater.* **2002**, *12*, 687−692.

(66) Roy, S. C.; Harding, A. W.; Russell, A. E.; Thomas, K. M. *J. Electrochem. Soc.* **1997**, *144*, 2323−2328.

(67) Sidik, R. A.; Anderson, A. B.; Subramanian, N. P.; Kumaraguru, S. P.; Popov, B. N. *J. Phys. Chem. B* **2006**, *110*, 1787−1793.

(68) Jaouen, F.; Lefèvre, M.; Dodelet, J.-P.; Cai, M. *J. Phys. Chem. B* **2006**, *110*, 5553−5558.

(69) Chisaka, M.; Iijima, T.; Tomita, A.; Yaguchi, T.; Sakurai, Y. *J. Electrochem. Soc.* **2010**, *157*, B1701−B1706.

(70) Schüth, F. *Angew. Chem., Int. Ed.* **2003**, *42*, 3604−3622.

(71) Lu, A. H.; Schüth, F. *Adv. Mater.* **2006**, *18*, 1793−1805.

(72) Weidenthaler, C.; Lu, A.-H.; Schmidt, W.; Schüth, F. *Microporous Mesoporous Mater.* **2006**, *88*, 238−243.

(73) Groen, J. C.; Peffer, L. A. A.; Pérez-Ramírez, J. *Microporous Mesoporous Mater.* **2003**, *60*, 1−17.

(74) Groen, J. C.; Pérez-Ramírez, J. *Appl. Catal., A* **2004**, *268*, 121−125.

(75) Arrigo, R.; Havecker, M.; Schlögl, R.; Su, D. S. *Chem. Commun.* **2008**, 4891−4893.

(76) Nesselberger, M.; Ashton, S.; Meier, J. C.; Katsounaros, I.; Mayrhofer, K. J. J.; Arenz, M. *J. Am. Chem. Soc.* **2011**, *133*, 17428−17433.

(77) Mayrhofer, K. J. J.; Strmcnik, D.; Blizanac, B. B.; Stamenkovic, V.; Arenz, M.; Markovic, N. M. *Electrochim. Acta* **2008**, *53*, 3181−3188.

(78) Meier, J. C.; Galeano, C.; Katsounaros, I.; Witte, J.; Bongard, H. J.; Topalov, A. A.; Baldizzone, C.; Mezzavilla, S.; Schüth, F.; Mayrhofer, K. J. J. *Beilstein J. Nanotechnol.* **2014**, *5*, 44−67.

(79) Mayrhofer, K. J. J.; Arenz, M.; Blizanac, B. B.; Stamenkovic, V.; Ross, P. N.; Markovic, N. M. *Electrochim. Acta* **2005**, *50*, 5144−5154.

(80) Arenz, M.; Mayrhofer, K. J. J.; Stamenkovic, V.; Blizanac, B. B.; Tomoyuki, T.; Ross, P. N.; Markovic, N. M. *J. Am. Chem. Soc.* **2005**, *127*, 6819−6829.

(81) Perez-Alonso, F. J.; Elkjær, C. F.; Shim, S. S.; Abrams, B. L.; Stephens, I. E. L.; Chorkendorff, I. *J. Power Sources* **2011**, *196*, 6085−6091.

(82) Topalov, A. A.; Katsounaros, I.; Auinger, M.; Cherevko, S.; Meier, J. C.; Klemm, S. O.; Mayrhofer, K. J. J. *Angew. Chem., Int. Ed.* **2012**, *51*, 12613−12615.

(83) Topalov, A. A.; Katsounaros, I.; Meier, J. C.; Klemm, S. O.; Mayrhofer, K. J. J. *Rev. Sci. Instrum.* **2011**, *82*, 114103−114105.

(84) Mayrhofer, K. J. J.; Ashton, S. J.; Meier, J. C.; Wiberg, G. K. H.; Hanzlik, M.; Arenz, M. *J. Power Sources* **2008**, *185*, 734−739.

(85) Mayrhofer, K. J. J.; Meier, J. C.; Ashton, S. J.; Wiberg, G. K. H.; Kraus, F.; Hanzlik, M.; Arenz, M. *Electrochem. Commun.* **2008**, *10*, 1144−1147.